Environmental Science Nano

Influence of Sensor Composition on Nanoparticle and Protein Interaction with Supported Lipid Bilayers

Journal:	*Environmental Science: Nano*
Manuscript ID	EN-ART-06-2023-000406.R1
Article Type:	Paper

Influence of Sensor Composition on Nanoparticle and Protein Interaction with Supported Lipid Bilayers

Christian A. Reardon-Lochbaum,[1] Ravithree D. Senanayake,[2] Rocio Amaro Marquez,[2] Kha Trinh,[2] Khoi Nguyen L. Hoang,[3] Tobias Rangel Guillen,[1] Catherine J. Murphy,[3] Robert J. Hamers,[1] Joel A. Pedersen[1,4,†] and Rigoberto Hernandez[2,5,*]

[1]Department of Chemistry, University of Wisconsin−Madison, 1101 University Avenue, Madison, Wisconsin 53706, United States

[2]Department of Chemistry, Johns Hopkins University, Baltimore, Maryland 21218, USA

[3]Department of Chemistry, University of Illinois at Urbana-Champaign, 600 South Mathews Avenue, Urbana, Illinois 61801, United States.

[4]Departments of Soil Science and Civil & Environmental Engineering, University of Wisconsin−Madison, 1525 Observatory Dive, Madison, Wisconsin 53706, United States

[5]Departments of Chemical and Biomolecular Engineering, and Materials Science and Engineering, Johns Hopkins University, Baltimore, Maryland 21218, USA

ABSTRACT: Supported lipid bilayers are often used as model systems for studying interactions of biological membranes with protein or nanoparticles. A supported lipid bilayer is a phospholipid bilayer built on a solid substrate. The latter is typically made of silica or a metal oxide due to the ease of its formation and range of compatible measurement techniques. Recently, a solvent-assisted method involving supported lipid bilayer formation has allowed the extension of compatible substrate materials to include noble metals such as gold. Here, we examine the influence of substrate composition (SiO_2 *vs* Au) on the interactions between anionic ligand-coated Au nanoparticles or cytochrome *c* and zwitterionic supported lipid bilayers using quartz crystal microbalance with dissipation monitoring. We find that anionic nanoparticles and cytochrome *c* have higher adsorption to bilayers formed on Au relative to those on SiO_2 substrates. We examine the substrate-dependence of nanoparticle adsorption with DLVO theory and all-atom

† Posthumous author; died on June 30, 2022.

* Corresponding author: r.hernandez@jhu.edu

simulations, and find that the stronger attractive van der Waals and weaker repulsive electrostatic forces between anionic nanoparticles and Au substrates *vs* anionic nanoparticles and SiO_2 substrates could be responsible for the change in adsorption observed. Our results also indicate that the underlying substrate material influences the degree to which nanoscale analytes interact with supported lipid bilayers; therefore, interpretation of the supported lipid bilayer model system should be conducted with understanding of support properties.

ENVIRONMENTAL IMPACT STATEMENT: Supported lipid bilayers are used as models to understand interactions of nanoscale analytes with cell membranes. We report differences between nanoparticle and protein adsorption to bilayers built on SiO_2 or Au solid supports and determine the degree to which they simulate environmentally relevant membranes. This work offers guidance in the interpretation of nanoscale analyte interactions with supported lipid bilayers and provides a basis for the development and refinement of environmental model systems.

KEYWORDS: quartz crystal microbalance with dissipation monitoring (QCM-D), supported lipid bilayer (SLB), solvent-assisted bilayer formation, cytochrome *c*, nanoparticle, DLVO theory, nonequilibrium molecular dynamics

INTRODUCTION

Supported lipid bilayers (SLBs) are often used as model systems for revealing the interactions of nanoscale analytes—such as protein,[1] pathogens,[2] or nanoparticles[3]—with cellular membranes. While relatively simple in comparison to nature's bilayers such as cell membranes, supported lipid bilayers are often selected due to their ease of use and compatibility with a number of analytical techniques capable of monitoring changes to the bilayer.[4] This list includes quartz crystal microbalance with dissipation monitoring (QCM-D),[5,6] localized surface plasmon resonance sensing (nano-plasmonic sensing),[7] atomic force microscopy,[8] infrared spectroscopy,[9] optical waveguide light mode spectroscopy,[10] and fluorescence imaging.[11,12] Individual monitoring techniques may necessitate specific measurement conditions or sensor composition. For example, to monitor bilayer properties with Fourier transform infrared spectroscopy, a bilayer must be formed on an internal reflection element commonly made of germanium,[13] zinc selenide,[14] or silicon;[15] meanwhile, monitoring bilayer properties with QCM-D requires a finely-made

piezoelectric sensor often coated with a metal oxide or gold.[6] Due to the array of analytical techniques used to monitor analyte interaction with SLBs, and subsequently the array of substrates required for different techniques, interpretation of SLB-analyte interaction requires an understanding of the influence that substrates have on SLB behavior.

The advantages of the vesicle fusion method of SLB formation include the ease with which it can be performed, and its compatibility with silicon dioxide (SiO_2) and silicon nitride (Si_3N_4) substrates that are in turn compatible with a wide range of measurement techniques.[7,10,12,16,17] To perform vesicle fusion, vesicles are exposed to a substrate until a critical surface concentration is reached, whereupon vesicles fuse and rupture to form a uniform supported lipid bilayer. The rupture of vesicles is facilitated by the hydrophilic character of the substrate; therefore, vesicle fusion necessitates a surface with relatively high hydrophilicity as is commonly found in metal oxides.[17,18] Unfortunately, the prevalence of the vesicle fusion technique for the formation of SLBs has limited systematic studies of the influence of substrate properties on bilayer-analyte interaction. A second method for SLB formation is the solvent-assisted method[18,19] which utilizes the self-assembly of a bilayer during an exchange from organic solvent to aqueous media. The solvent-assisted method has recently been used to make SLBs on both Au and SiO_2 substrates,[19–21] and offers an opportunity to compare nanoscale analyte interaction with SLBs built on both substrates. To this end, Ferhan et al[19] found that more streptavidin was observed to adsorb to SLBs on Au than on SiO_2. (Note that the behavior referred to in this work as adsorption is also known as deposition in the surface science literature.) To date, robust analysis of the difference in adsorption character between SLBs formed on SiO_2 *vs* Au substrates has not been performed.

Here, we investigate the difference in the interactions of analytes, anionic nanoparticles and proteins, with supported lipid bilayers formed on SiO_2 and Au surfaces as illustrated in Figure 1. We compare interactions of anionic 11-mercaptoundecanoic acid functionalized gold nanoparticles (MUA-AuNPs) and cytochrome *c* with a variety of SLBs. Gold nanoparticles (AuNPs) are commonly used as a benchmark for revealing properties at the nano-bio interface because of the former's tunability in size and surface charge, and their ready quantitative detection within biological systems after extraction *via* inductively-coupled plasma mass spectrometry.[22] Mercaptoundecanoic acid is an

anionic ligand that has been placed on 4 nm AuNPs as a model anionic particle, and has previously been used to study NP–bilayer interaction.[23] Cytochrome *c* is a model peripheral membrane protein that has previously been incorporated into supported lipid bilayers of varying lipid composition.[24] Cytochrome *c* adsorption and incorporation into SLBs is dependent on both the contact orientation final orientation of the protein with the bilayer.[24–26] Cytochrome *c* associates with the inner mitochondrial membrane and is a key component to mitochondrial membrane function.[27] We chose cytochrome c in the work so as to further reveal the influence of substrate on protein-bilayer interactions because it is an established benchmark for describing the interactions between a protein and a bilayer[28] and for nonspecific protein-lipid interactions.[29] We compare interactions of MUA functionalized AuNPs and cytochrome *c* with SLBs formed on SiO_2 *vs* Au substrates to determine the effect of substrate composition on nanoparticle or protein-bilayer interaction. We find that negatively charged MUA-AuNPs and cytochrome c interact more strongly with SLBs formed on Au than SiO_2 substrates. We analyze the AuNP–SLB interactions with extended DLVO theory, and find that the larger Hamaker constant, representing an increase in van der Waals attractive forces between the substrate and AuNP, for AuNP–Au interaction as opposed to AuNP–SiO_2 interaction can account for some of the change in interaction. We use nonequilibrium molecular dynamics simulations[30,31] to observe the relative interactions and binding of Cytochrome *c* to the surface of the bilayer in comparison to the SLBs. Note that that the relaxation of the initial unbiased position of the protein far—but not too far—from the surface is the nonequilibrium process of interest. Combined, our results suggest that long-range Coulombic repulsion between the SiO_2 substrate and negatively charged analytes may account for some of the observed changes in the structure and interaction of the protein with the SLBs. We conclude that substrate properties are the reason for increased interaction between negatively charged nanomaterial or protein and zwitterionic SLBs. We expect that these results will inform the choice of substrate in future studies modeling specific biological systems.

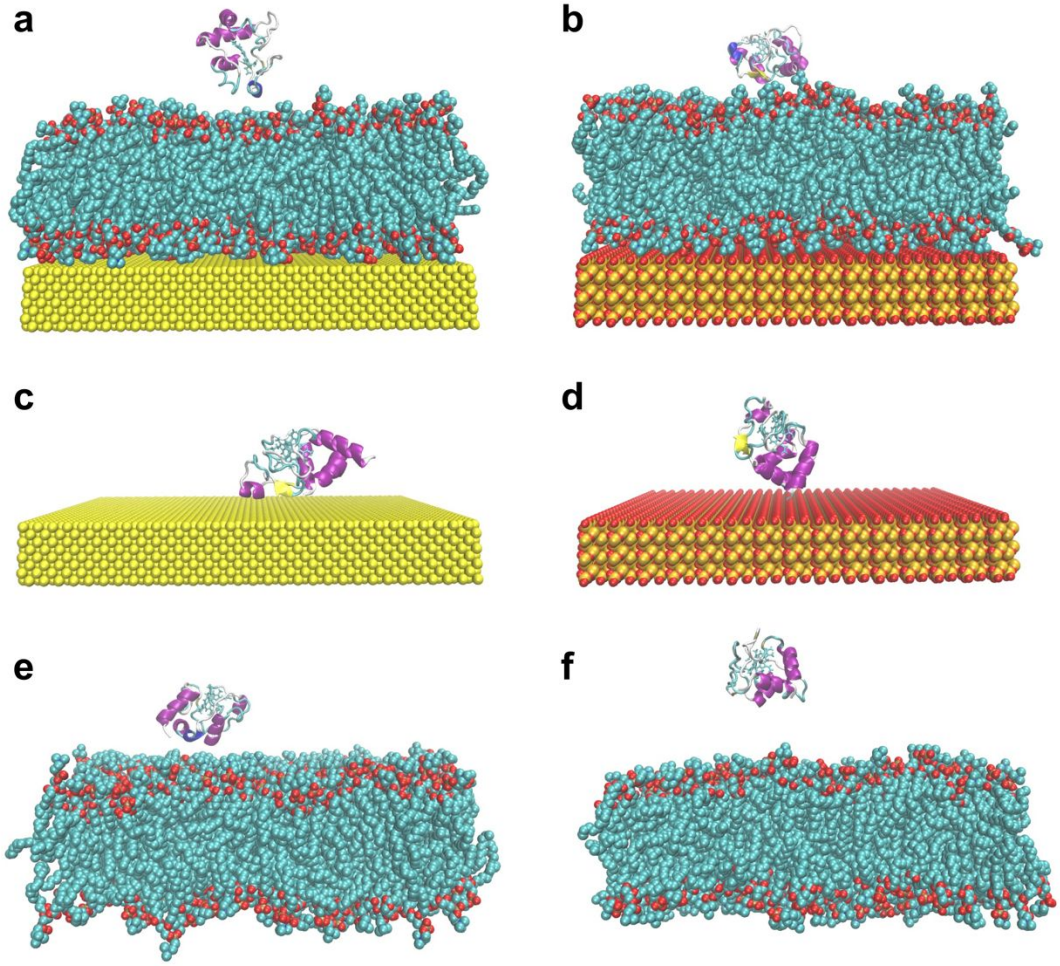

Figure 1. The snapshots taken from cytochrome c-SLB composite systems of Au(100) and SiO_2 surfaces and the control experiment simulations. a) cytochrome c with Au(100)-SLB b) cytochrome c with SiO_2-SLB c) cytochrome c with Au(100) d) cytochrome c with SiO_2 e) and f) cytochrome c with DOPC lipid bilyer. C: cyan, O: red, N: blue, Au(100): yellow, Si: orange. Water molecules, hydrogen atoms, Na^+ and Cl^- ions are removed for clarity.

MATERIALS AND METHODS

Materials. We purchased the zwitterionic phospholipid, 1,2-dioleoyl-*sn*-glycero-3-phosphocholine (DOPC) from Avanti Polar Lipids. We procured 2-[4-(2-hydroxyethyl)piperazin-1-yl] ethanesulfonic acid (HEPES) and NaCl from Fisher Scientific. All aqueous solutions were prepared in ultrapure water (18.2 MΩ·cm,

Barnstead Nanopure). Aqueous buffer solutions were prepared with 10 mM HEPES and buffered to pH 7.4, unless otherwise noted. Isopropanol (HPLC grade) was purchased from Spectrum Chemical (product number HP692). Tetrachloroauric (III) acid (≥ 99% trace metal basis), tannic acid (ACS reagent), potassium carbonate (ACS Reagent), and 11-Mercaptoundecanoic acid (MUA) (95%) were purchased from Sigma-Aldrich, trisodium citrate dihydrate was purchased from Flinn Scientific.

Equine heart cytochrome *c* (M_r =12,384) was obtained from Sigma-Aldrich. Cytochrome *c* was dissolved in 10 mM NaCl at a stock concentration of 5 mg·mL^{-1}. Cytochrome *c* stock solution was stored at −20 °C and thawed a maximum of once per aliquot. Cytochrome c stock was diluted to 0.05 mg·mL^{-1} in 10 mM NaCl for QCM-D experiments.

Nanoparticle Synthesis. MUA-AuNPs (8 nm core diameter) were synthesized based on the generational growth method as reported by Piella *et al*.[32] Briefly, a seed solution is prepared by combining 150 mL of 2.2 mM sodium citrate, 0.1 mL of 2.5 mM tannic acid, and 1 mL 150 mM of potassium carbonate and heating to 70 C. Once the solution reaches 70 C, 1 mL of 25 mM tetrachloroauric acid is added. The solution is held at 70 C for 5 min to ensure complete reaction of the gold precursor. The seed solution is immediately used to grow AuNPs in the same reaction vessel. For each generational growth, 55 mL of the seed solution is removed and replaced by 55 mL of fresh 2.2 mM sodium citrate, followed by two injections of 0.5 mL of 25 mM $HAuCl_4$, which are added at 10-min time intervals. The desired core size of 8 nm was reached after three generations minus one $HAuCl_4$ injection. As synthesized AuNPs are conjugated with MUA by incubating with 0.1 mL of 1 mM MUA overnight on a commercial orbital shaker (viz, the Belly Dancer® from Sigma-Adrich).MUA-AuNPs are purified using a regenerated cellulose centrifugal filter (MWCO 10,0000, Amicon) at 15,000*g* for 15 min.

Nanoscale Material Characterization. Core size of MUA AuNPs is characterized by transmission electron microscopy (TEM) with a 2100 Cryo TEM (JEOL) with LaB_6 emitter operated at 200 keV. Ten µL of MUA-AuNPs suspended in water were drop-casted onto a Ted Pella copper grid with carbon type-B 300 mesh. Representative TEM images and average core diameter are shown in Figure S1 and Table S1, respectively. Average size and size distribution of the samples were measured using ImageJ software

by counting at least 200 particles. Hydrodynamic diameter of MUA AuNPs is characterized by UV-visible spectra with a Carry 5000 UV-Vis NIR (Agilent Technologies) using a 1 ml glass cuvette in the range from 400-800 nm. Spectra of MUA AuNP localized surface plasmon (LSPR), which is used to calculate the hydrodynamic diameter,[33] are shown in Figure S2.

Hydrodynamic diameter and zeta potential of the nanoscale materials used are characterized with a Malvern Zetasizer. The Zetasizer measures diffusion coefficients and electrophoretic mobility by dynamic light scattering (DLS) and laser Doppler electrophoresis (LDE), respectively, and converts to hydrodynamic diameter and zeta potential using the Stokes-Einstein[34] and Henry[35] equations, respectively. These calculations rely on the assumption that measured nanoscale materials are spherical. Hydrodynamic diameter and zeta potential for nanoscale materials are reported in Table S1. Vesicles and MUA AuNPs are measured in 150 mM NaCl. Cytochrome *c* is measured in 100 mM NaCl. Average and error for hydrodynamic diameter and zeta potential are taken from 10 and 12 replicate measurements, respectively.

Quartz Crystal Microbalance with Dissipation Monitoring. Quartz crystal microbalance with dissipation monitoring was performed with a Q-Sense Analyzer. Sensors were purchased from Biolin Scientific (SiO_2 QSX 303; Au QSX 301). As per manufacturer, SiO_2 sensors have a 10 nm chromium layer, 100 nm Au layer, 20 nm Ti, and 50 nm SiO_2 layers. Au sensors have a 10 nm chromium layer coated in 100 nm of Au. Coating is performed by the manufacturer by physical vapor deposition, which leaves an SiO_2[36] or Au(111)[37] surface, respectively. Sensors were used as received and reused a maximum of 5 times. Between uses, sensors were cleaned with 2% sodium dodecyl sulfate, thoroughly rinsed with ultrapure water, dried over N_2, and treated with ozone for 20 min. Cleaning with ozone followed by rinse with water has been shown to remove oxides and leave bare Au or Si surfaces.[36,38] Before every experiment, 150 mM NaCl was flowed over sensors until a stable baseline formed. Unless otherwise noted, all flow speeds were 100 $\mu L \cdot min^{-1}$. All analysis was performed with the 5th harmonic.

Supported Lipid Bilayer Formation. All SLBs were formed with zwitterionic 1,2-dioleoyl-sn-glycero-3-phosphocholine (DOPC). Vesicle fusion SLBs were made by the vesicle fusion method on SiO_2 substrates as reported by Cho *et al*.[17] In short, vesicles

were formed by drying lipid in glass container over vacuum, sonicating for 30 min, 3-5 min freeze/thaw cycles in liquid N_2, and 11 extrusions through 50 nm polycarbonate filters. Vesicle hydrodynamic diameter and zeta potential were determined by DLS and LDE (Table S1). After formation, vesicles were stored at 4 °C for a maximum of 10 days before use. Vesicle fusion bilayers were formed by treating SiO_2 sensors with ozone for 20 min, then flowing 0.125 mg·mL^{-1} DOPC vesicles over sensors in 150 mM NaCl until a critical surface concentration was reached on the sensor surface and spontaneous rupture occurred. Frequency and dissipation vs time, for vesicle fusion bilayer formation, is shown in Figure S3a. Final frequency and dissipation for vesicle fusion bilayers is reported in Table S2.

Solvent-assisted SLBs were made by the solvent-assisted method on Au and SiO_2 substrates as reported by Ferhan *et al*.[19] Sensors were treated with 20 min of ozone immediately before lipid flow. In short, 0.5 mg·mL^{-1} DOPC in isopropanol was flowed over sensors for 20 min. Isopropanol was exchanged with 150 mM NaCl at a flow rate of 50 µL·min^{-1} until a stable baseline occurred. Frequency and dissipation vs time for solvent assisted bilayer formation is shown in Figures S3b and S3c.

Final frequency and dissipation for bilayers was taken as the average of 5 minutes of 150 mM NaCl buffer flow after a stable baseline was achieved. The frequency and dissipation for SLBs are consistent with previously reported bilayers formed on SiO_2 and Au with both formation techniques,[39] and are tabulated in Table S2. The reported values and error for frequency and dissipation of bilayers were taken from 8 replicate measurements. All subsequent bilayers used in this work fell within the respective ranges for frequency and dissipation as reported in Table S2.

Nanoparticle and Protein Interaction with Bilayers. Anionic MUA-AuNP interaction with SLBs was carried out as reported by Chong *et al*.[23] In short, after the formation of a SLB, 3 nM MUA-AuNPs suspended in 150 mM NaCl were flowed for 20 min. After 20 min of flow, bilayers were rinsed with 150 mM NaCl until a stable baseline formed.

Cytochrome *c* interaction with SLBs was carried out as reported by Melby *et al*.[24] In short, 100 mM NaCl was flowed over SLBs until a stable baseline was formed. The flow rate was slowed to 50 µL·min^{-1}, then 0.05 mg·mL^{-1} cytochrome *c* was introduced for

30 min of flow. After 30 min of continuous cytochrome *c* flow, the pump was stopped for 30 min. The reduced flow speed of cytochrome *c* interaction and period of flow stop, allows for cytochrome *c* adsorption and relaxation on the bilayer. Finally, the bilayer was rinsed with 100 mM NaCl until a stable baseline formed.

DLVO Theory for Substrate-Bilayer-NP Interaction. We use the theory of colloidal suspension developed by Derjaguin, Landau, Verwey, and Overbeek—known as DLVO theory—to predict relative interaction energies of nanoparticles with surfaces.[40,41] Here, we have used the equations derived by Hogg *et al.*[42] adapted for a spherical particle interacting with a planar surface by Hahn and O'Melia.[40] In DLVO theory, van der Waals forces are broken down into contributions from three distinct sources: orientation forces, Debye induction force, and London dispersion force.[40,43,44] The contributions from these forces can extend as far into solution as 10 nm.[45] In addition to classical DLVO forces, several extensions to DLVO theory can be applied to include contributions from surface hydration, Born repulsion, hydrophobicity, etc.[40,43,44]

For a given interaction, the total energy of interaction (W_{tot}) is equal to the energies of van der Waals (W_{vdW}), Coulombic (W_C) interactions, and Born forces (W_B). The interaction energies are all a function of distance (d) between two surfaces.

$$W_{tot} = W_{VdW} + W_C + W_B \quad (1)$$

The van der Waals interaction energy between a particle and flat surface is described as a function of distance (d) between the two surfaces:

$$W_{VdW} = \frac{-rA_{12}}{3d}\left(1 + \frac{14d}{\lambda}\right)^{-1} \quad (2)$$

Where r is the particle radius, A_{12} is the Hamaker constant for the interaction between two surfaces through a defined medium, and λ is the characteristic decay wavelength. For the MUA-AuNPs, r was taken to be 4 nm, half the measured hydrodynamic diameter, which is attributed to both core and ligand shell diameter (Table S1). The decay wavelength was taken to be 100 nm.[40] The Hamaker constant for the interaction between two surfaces (A_1 and A_2) through a given medium (A_m) can be approximated using Lifshitz theory.[45]

$$A_{12} = (\sqrt{A_1} - \sqrt{A_m})(\sqrt{A_2} - \sqrt{A_m}) \quad (3)$$

Given the Hamaker constants of individual system components, substrate, medium, SLB, and NP, we can estimate the Hamaker constants of interaction and estimate the van der Waals interaction energy. Constants for each interaction can be found in Table S4.

The energy of Coulombic interaction between a particle and a flat surface is described as:

$$W_C = 2\pi\epsilon_0\epsilon_r r\left[2\psi_1\psi_2 \ln\left(\frac{1+\exp(-\kappa d)}{1-\exp(-\kappa d)}\right) + \left(\psi_1{}^2 + \psi_2{}^2\right)\ln(1-\exp(-\kappa d))\right] \quad (4)$$

Where ϵ_0 is the permittivity of free space, ϵ_r is the relative permittivity of the medium, ψ is the surface potential, and κ is the inverse Debye length. Constants for these calculations can be found in Table S5. We can experimentally determine the zeta potential (ζ) of particles and surfaces, which can be converted to a surface potential (ψ).[41]

$$\psi = \zeta\left(1 + \frac{z}{r}\right)\exp(\kappa z) \quad (5)$$

Where z is the thickness of the hydration layer traveling with the particle and κz is the ratio of the Debye length (κ^{-1}) to the thickness of the hydration layer (z). The thickness of the hydration layer was taken as 3 Å: approximately two atomic layers of water.[43] Equation 5 relies on assumptions of spherical particles in solution. For planar substrates, r is taken to be infinitely large. Zeta potentials used to estimate surface potentials can be found in Table S6. Specifically, the zeta potentials of planar bilayers were approximated by the zeta potential of 100 nm vesicles in solution.

The Debye length (κ^{-1}) is the characteristic length over which the electrostatic potential decays:

$$\kappa^{-1} = \frac{k_B T}{4\pi e_i^2 \sum v_i^2 n_i} \quad (6)$$

where ε is the dielectric constant of the liquid medium. For a solution with i ionic species in bulk solution, v_i is the valency and n_i is the number concentration of ionic species i. The double layer thickness, and in turn the zeta potential, is a function of the ionic strength of solution.

We have included an extension to classical DLVO theory using the Born repulsion energy (W_B). Born repulsion accounts for the large repulsive force between two surfaces at small interfacial distances. Born repulsion is:

$$W_{\mathrm{B}} = \frac{rA_{12}\sigma^6}{3780}\left(\frac{16r+d}{(4r+d)^7} + \frac{12r-d}{d^7}\right) \quad (7)$$

where σ is the Born collision diameter, which has been defined as 0.5 nm.

Using equations 1, 2, 4, and 7, the interaction energy between a substrate (SiO_2 or Au) and a nanoparticle, substrate and a bilayer, or bilayer and a nanoparticle as a function of separation distance are calculated. The calculated interaction energies are compared to experimentally determined adsorption.

Molecular Dynamics Simulations. *Simulation Setup***.** The peripheral membrane protein cytochrome *c* and 1,2-Dioleoyl-sn-glycero-3-phosphocholine (DOPC) lipid bilayers are pre-equilibrated in an all-atom water solvent (described below) prior to combining them with an inorganic slab, a lipid bilayer, or a supported lipid bilayer (SLB). SLBs with Au(100), Au(111) and SiO_2 inorganic supports are constructed with pre-equilibrated DOPC lipid bilayers; refer to the structures shown in Figure S4. As in the experiments, the inorganic slabs upon exposure to SiO_2 are functionalized with silanols (13.3% ionized at pH=7.4) to stabilize the DOPC lipid bilayers on the surface. Two structures for each of the three target SLBs can be constructed by positioning the bilayer at average distances of 1.5 nm and 1 nm between the bottom of the bilayer and the surface of the inorganic slab filled with an all-atom water solvent. A third structure was found to be necessary for the stabilization of the SLB with Au(111) support in which the lipid bilayer was positioned with an effective distance of 0.7 nm between the bottom of the bilayer and the surface of the inorganic slab as the structure with the bilayer positioned at the default distances did not remain stable.

The SLBs with cytochrome *c* are constructed with a pre-equilibrated cytochrome *c* protein inserted with its lowest point above the surface of the SLB at 20 Å. Thus, the distance from the closest top surface of the SLB to the COM of the protein is ~33.6 Å given that the radius of the cytochrome *c* is 13.6 Å.[46] In order to sample the orientation space of the protein, six orientations differing from each other by 90° rotations in reference to the SLB surface (Figure S5) are used as the initial conditions. A similar approach to

sampling this orientation space was used earlier by some of us in characterizing cytochrome *c* near lipid bilayers and negatively charged 3-mercaptopropionic acid coated gold nanoparticles.[24,47] Therein, we found that such a sampling approach provided a reasonable representation of the ensemble of structures sampled by the highly anisotropic protein close to a flat surface. In the present work, its use required six simulations for each of three different SLB systems: Au(100)-SLB, Au(111)-SLB and SiO_2-SLB. In addition, four sets of control simulations were performed: cytochrome *c* was placed near the surface of a DOPC lipid bilayer, and that of pure slabs of Au(100), Au(111) and SiO_2. Each set was sampled at six different initial relative orientations of the protein at a distance from the surface as was performed for the SLBs.

The DOPC lipid bilayers and inorganic slabs [Au(100), Au(111) and SiO_2] have been modeled with the membrane builder[48] and nanomaterial modeler[49] available in CHARMM-GUI[47] and Visual molecular dynamics (VMD).[51] In building the SLBs, Packmol[52] and VMD tcl scripting were used to pack and align the protein and lipid bilayer with inorganic surfaces. SLBs without cytochrome *c*, SLBs with cytochrome c and control experiments are solvated using TIP3P[53] water and ionized with 0.01 M NaCl using VMD.[51] The box dimensions are set to [126 Å x 126 Å x 240 Å], [126.8 Å x 125 Å x 240 Å], and [121 Å x 127 Å x 240 Å] for the systems containing Au(100), Au(111), and SiO_2 respectively. The box dimensions of the control experiments for cytochrome *c* with DOPC lipid bilayer are set to 121 Å x 127 Å x 240 Å. In all cases, cytochrome *c* is centered at the *x*-*y* plane of the box near the closest top surface. During the simulations, the inorganic slabs are fixed, and the lipid and the cytochrome c are set to relax.

Simulation parameters, equilibration, and production simulations. All-atom simulations of SLBs with and without cytochrome *c* and the control experiments are run using the Nanoscale Molecular Dynamics program, version 2.14 (NAMD 2.14).[54] The interactions involving cytochrome c and DOPC lipids are modeled using all-atom CHARMM36 force fields.[55] The INTERFACE force field[56] has been used to model the FCC gold and SiO_2 surfaces. A Langevin thermostat with a 5 ps^{-1} damping constant ensures constant temperature. A Langevin piston with a period of 1 ps and a decay rate of 50 fs ensures constant pressure. The SHAKE algorithm ensured that bonds involving hydrogen bonds are fixed during all simulations. Nonbonded interactions between atoms

within three bonds of each other and atoms further than 12 Å from each other are presumed to be zero and were not included in the calculated forces. The particle mesh Ewald method with a grid spacing of 1.0 Å describes the long-range electrostatics. A smoothing function is applied to pairs of atoms between 8 and 12 Å. All systems are propagated with a 2 fs timestep unless otherwise stated, and periodic boundary conditions were applied in all simulations.

The analyte-SLB composite systems (Figure 1) were equilibrated in a multistep process. First, the system was subjected to 1,800,000 steps of conjugate gradient minimization. Then, in the systems involving DOPC lipid, the lipid was restrained in the *z* direction to equilibrate lipid in *xy* direction for 9 ns *NPT* (1 fs timestep, 1 atm, 300 K) before the full equilibration. Note that the lipid restraint was performed to stabilize the lipid on the solid substrate without any lipid deformations. In a subsequent (second) *NPT* simulation without the lipid restraint, the lipid was fully equilibrated for another 4.5 ns *NPT* (1 fs timestep, 1 atm, 300 K) simulation. For those systems without lipid bilayer-substrate interactions, only one initial 1.5 ns *NPT* (1 fs timestep, 1 atm, 300 K) simulation was performed.

Volume scaling was allowed along the longest axis of the periodic box in the flat surface simulations. The temperature was initialized at 5 K and was permitted to increase smoothly to 300 K. Then, the systems were minimized for 3000 more steps to remove bad contacts between different periodic copies of the inorganic slabs and lipids. In the second step, the SLB systems were reheated to 300 K in an *NVT* step. The constraints on systems were progressively decreased over 1.8 ps, followed by 3 ns of equilibration with no constraints to lipid and protein. Each simulation was run for an additional 100 ns production in the *NVT* ensemble.

Numerical measurements seen from the simulations. To understand the analyte-SLB interactions, the COM of four proposed binding sites[47] of cytochrome *c* (A, C, L, and N) and the COM of the entire protein were tracked during the simulations. VMD's NAMD energy plugin[51] is used to calculate the interaction energies—for hydrogen bonded and non-bonded atoms—within a cytochrome *c,* and between it and the bilayers or the inorganic slabs. Various protein configurations are sampled, and hence averaged protein densities are used to describe the protein–SLB interaction. The radius of gyration (*R*g) of

a cytochrome *c* near SLB surfaces is monitored to reveal possible structural differences in the protein due to the interactions with SLBs or surfaces. The numerical measurements are carried out using the endmost 80 ns from each trajectory wherein the systems were seen to be equilibrated. The post-processing of data and analysis is performed using tcl scripting in VMD and Python numpy[57] with Jupyter notebooks.[58]

RESULTS AND DISCUSSION

Bilayer Formation Method Effects on Nanoparticle and Protein Interaction. The traces of frequency and dissipation *vs* time for the formation of bilayers formed during vesicle fusion on SiO_2 and solvent displacement on SiO_2 or Au were measured experimentally, and are available in Figure S3 and Table S2. There is no difference between the frequency and dissipation values of the vesicle fusion bilayers or solvent-assisted bilayers formed on SiO_2 ($p > 0.05$). This is in agreement with a previous report comparing the two methods.[19] The solvent-assisted bilayers formed on Au have a larger frequency shift than those formed on SiO_2 (–28 ± 2 and –24 ± 1 Hz, respectively). The increased frequency of solvent-assisted bilayers formed on Au *vs* SiO_2 is in agreement with the previous report.[19] The increase in frequency shift of a SLB on Au *vs* SiO_2 is attributed to an increase in the hydration layer coupled to the Au surface.[19] The dissipation is the same for solvent-assisted bilayers regardless of substrate ($p > 0.05$). The similarity in the frequency and dissipation of bilayers formed on SiO_2 vs. Au allows for the direct comparison of analyte adsorption to bilayers formed on either substrate.

The frequency and dissipation change for MUA-AuNP and cytochrome *c* interaction with DOPC bilayers, formed by both the vesicle fusion and solvent-assisted methods, on SiO_2 substrates are available in Table S3. We observe no attachment of either anionic AuNPs or cytochrome *c* to bilayers on SiO_2 regardless of formation method. We take the similar degree of interaction between analytes and bilayers, or lack thereof, on the same substrate regardless of formation method as further confirmation that the bilayer formation technique does not affect bilayer properties.

Substrate Effects on Nanoparticle Bilayer Interaction. Figure 2 shows the frequency and dissipation change for 20 min of MUA-AuNP flow over bare SiO_2 and Au surfaces, as well as single component DOPC SLBs, formed on SiO_2 and Au surfaces, and subsequent rinse. Final frequency and dissipation change after rinse is also reported

in Table S3. A negative change in frequency corresponds with increased mass deposition or adsorption of AuNPs to the bilayer. A positive change in dissipation corresponds with a decrease in rigidity of the coupling of deposited material to the oscillating sensor surface. We find no interaction between MUA-AuNPs and bare SiO_2 or DOPC SLBs formed on SiO_2 surfaces, resulting in zero detectable frequency or dissipation change ($p < 0.05$). This observation is consistent with previous observation of MUA-AuNPs and a similar SLB system.[23]

In contrast, MUA-AuNPs adsorb to both bare Au sensors and SLBs formed on Au sensors. The magnitude of frequency change was larger for SLBs on Au surfaces as compared to bare Au surfaces. The AuNP adsorption to bare Au did not increase energy dissipation, consistent with tightly coupled adsorption of NPs to a surface.[59] The AuNP adsorption to SLBs on Au surfaces caused an increase in energy dissipation, indicating AuNPs are more rigidly adsorbed to bare Au surfaces than to SLBs.[60] In a similar system with AuNPs interacting with lipid vesicles, some of us—viz Chong et al.[23]—found that MUA-AuNPs interact with DOPC lipid in molecular dynamics while seeing no detectable interaction in QCM-D. In the experiments of the present work, we now see MUA-AuNPs interacting with SLBs formed on Au surfaces well in alignment with the earlier computational findings.

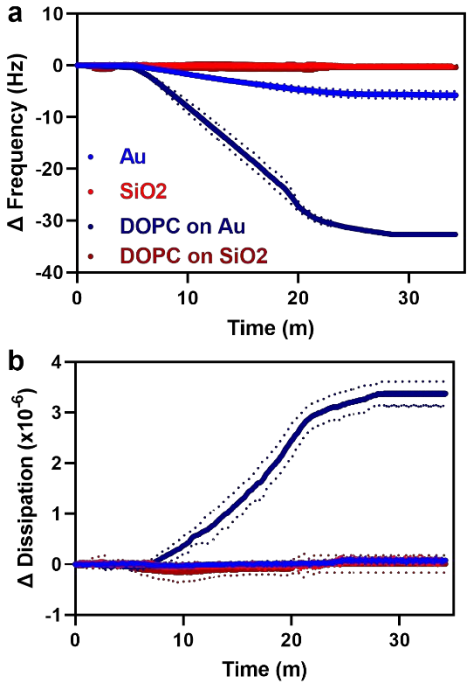

Figure 2. Change in (a) frequency and (b) dissipation *vs* time for interactions of MUA-AuNPs with bare Au, bare SiO_2, DOPC bilayer formed on Au, and DOPC bilayer formed on SiO_2. All SLBs are formed with the solvent-assisted method. Dotted lines represent one standard deviation of four replicate measurements.

DLVO Theory of AuNP Interactions. Adsorption of nanoscale analytes to a flat surface relies on two sequential steps: 1) mass transport of the analyte toward the surface and 2) adsorption of the analyte on the surface.[40] In aqueous phase, the mass transport of analyte to the surface can be described by diffusion, gravity, and—in the presence of an electric field—Coulombic repulsion or attraction. [40,61] The adsorption process can be described by Coulombic and van der Waals interactive forces through DLVO theory as detailed in Materials and Methods. Gold substrates provide an interesting comparison to SiO_2 because they carry negligible surface charge at neutral pH[62,63]—potentially changing the electrostatic interactions between SLBs and analytes—and have significantly higher attractive van der Waals interactions with many analytes.[64]

To determine if the difference between AuNP interaction with SiO_2 and Au substrates can be attributed to van der Waals or Coulombic forces, we analyze the interactions with extended DLVO theory. Our application of extended DLVO theory takes

into account van der Waals, Coulombic, and Born interactions.[44] We graph the interaction energy calculated with equation 1 *vs* the separation distance between a nanoparticle and surface. A negative interaction energy equates to an attractive interaction. Figure 3a shows the predicted interaction energies between AuNPs and bare SiO_2 or Au substrates. For our AuNP interacting with a bare SiO_2 surface, we predict repulsive forces will dominate the interaction within 10 nm of the surface. For our AuNP interacting with a bare Au surface, we predict attractive forces will dominate the interaction giving rise to a minimum energy position close to the surface.

Figure 3d shows a breakdown of interaction energies based on van der Waals or Coulombic interactions. We do not include a breakdown of Born interactions, as they are negligible except at small separation distances where they become repulsive. The primary contributor to AuNP interactions with SiO_2 is Coulombic repulsion, while attractive van der Waals interactions are not large enough to overcome this repulsion. In contrast, the Coulombic interaction between AuNPs and Au surfaces is negligible compared to the attractive van der Waals interactions. The Hamaker constant for interaction between a AuNP and Au surface is one order of magnitude larger than that for a AuNP and SiO_2 surface (Table S4). Additionally, the neutral Au surface has negligible Coulombic interaction with the anionic AuNP, whereas the anionic SiO_2 surface will repel the anionic AuNP. This is consistent with the AuNP adsorption to SiO_2 and Au surfaces observed in QCM-D experiments (Figure 2).

To calculate the interaction energy for substrate-SLB-AuNP interaction, we first calculate the substrate-SLB interaction energy (Figure 3b). For a SLB on SiO_2 substrate, a clear minimum energy position exists approximately 1.5 nm from the surface. This application of DLVO theory has previously been shown to be a good approximation of the SiO_2-SLB interaction and subsequent separation distance.[43] For a SLB on Au substrate, the minimum energy position is significantly deeper and closer to the surface, with this application of DLVO theory predicting stronger adsorption of the lipid to the Au *vs* SiO_2 surfaces. Figure 3e shows the strong adsorption of lipid to Au surface is a product of the large van der Waals attraction for the Au-DOPC interaction. The predicted adsorption of lipid to Au surface may also be indicative of the inability to form SLBs on Au surfaces with the vesicle fusion method and the anticipated change in SLB-substrate separation

distance for Au *vs* SiO_2 substrates.[19] To our knowledge, no direct measurement of Au-SLB separation distance has been performed. This measurement may provide more insight into the difference in adsorption behavior of AuNPs to different substrates.

Using the calculated distance from substrate surface to SLB lower leaflet (1.5 nm) and a predicted SLB thickness of 4 nm,[43] we calculate the interaction energy for a AuNP interacting with a SLB built on Au *vs* SiO_2 surfaces (Figure 3c). We predict the AuNPs will adsorb to SLBs built on both surfaces, with a slight increase in the depth of the minimum energy for a SLB on a Au surface. The close correspondence of calculated interaction energies is due to the diminishing substrate–AuNP interactions farther into solution. In this case, the substrate–SLB distance (1.5 nm) and thickness of a SLB (4 nm) encompass the majority of space where predicted interactions between the substrate and AuNP would occur. Figure 3f shows the small increase in attractive van der Waals interactions and negligible difference in Coulombic interaction for a AuNP-SLB interaction when built on Au vs SiO_2 surface. This is in contrast with the significantly increased adsorption of AuNPs to SLBs built on Au vs SiO_2 surface observed in QCM-D measurements (Figure 2). It is possible that forces acting on the AuNP outside of the calculated van der Waals, Coulombic, and Born interactions play a larger role in AuNP adsorption to a SLB than DLVO theory implies. For example, hydration or image charge forces on the system could be important although we have not calculated them. Hydration forces are net repulsive and increase in magnitude with increased surface charge density.[40,65] The magnitude of repulsion from hydration on the SiO2 surface, and the bilayer built on the SiO2 surface, would be greater than that of a Au surface. Forces from image charges, generated by spontaneous charge distributions near the substrate-solution interface, would constitute a net attractive force between a polarizable AuNP and a surface.[66,67] However, this force would be greater in magnitude for an anionic particle interacting with a neutral Au surface *vs* an anionic SiO_2 surface. Both of these forces may contribute to AuNP adsorption behavior, and the present omission of these forces could explain the remaining discrepancies between the experimental observations and the DLVO calculations.

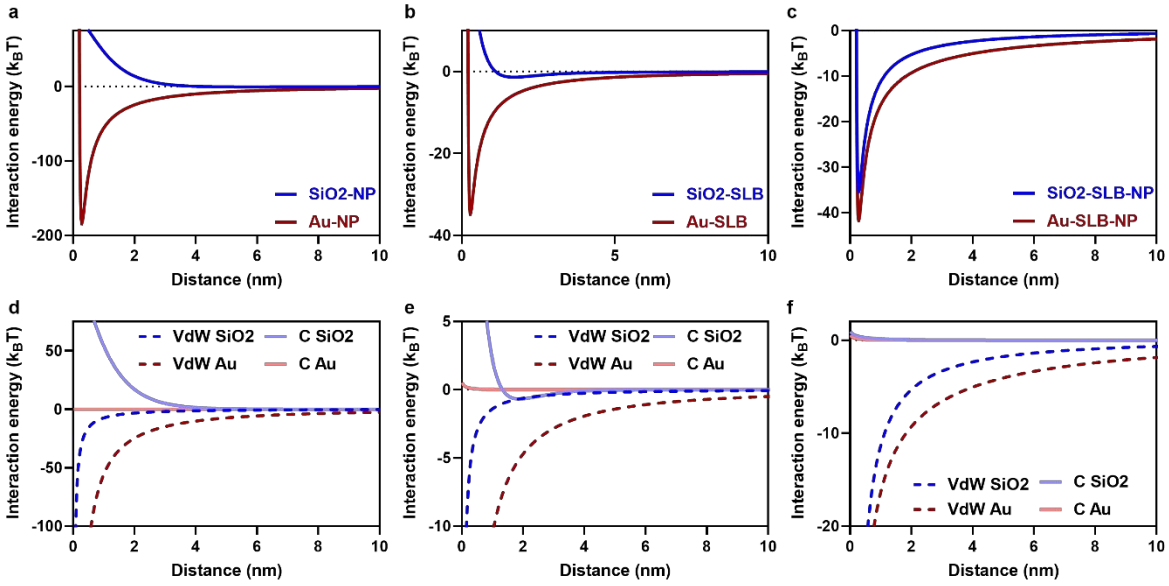

Figure 3. Calculated energies for (a) bare substrate-AuNP, (b) substrate-SLB, and (c) substrate-SLB-AuNP interaction using DLVO theory. Interaction energies are broken down into contribution from van der Waals (vdW; equation 2) and Coulombic (C; equation 4) interactions for (d) bare substrate-AuNP, (e) substrate-SLB, and (f) substrate-SLB-AuNP interaction. All calculations were performed with equations 1, 2, and 4 with constants used in Tables S4 and S5.

Behavior of Au(100), Au(111) and SiO_2 SLBs. The interactions between bilayers and substrates in SLBs were interrogated through simulations of bilayers supported on Au(100), Au(111), and SiO_2 substrates. For each such system, simulations with distinct box dimensions—specifically [85 Å x 85 Å x 240 Å] and [162 Å x 162 Å x 600 Å— were employed to ensure that results were unaffected by this choice. The effective distance between the lipid bilayer and supports is the thickness of the water thin film formed within the SLBs. When the effective distance between the lipid bilayer and the Au(100) surface was set to D=1.5 nm (Figure S4), the DOPC lipid bilayer tended to deform from the outset of the SLB simulations. This behavior was observed in lipid bilayers irrespective of the choice of simulation box sizes. This observation led to reduction of D to ~1 nm, which stabilized the DOPC lipid bilayer on a Au(100) support. An instability of the lipid bilayer was observed for the Au(111)-SLB with a D=1 or 1.5 nm. The lipid bilayer on Au(111) was stabilized only with a reduced thickness of D'=0.7 nm (Figure S4).

The DOPC lipid bilayer did not remain stable on the bare SiO_2 surface of the SiO_2-SLB when the thickness of the water film between them was initiated at *D* equal to a 1.5 nm effective distance. However, after the functionalization of SiO_2 with silanols (13.3% ionized at pH=7.4), the DOPC lipid bilayer was found to be stable with a film of this thickness, but significantly deformed (Figure S4). Reducing *D* to 1 nm stabilized the DOPC lipid bilayer on the SiO_2 support, and resulted in a lack of deformations. A similar water thin film thickness has been reported in a Muscovite(mica)-SLB formed with DOPC and DPPC lipid bilayers exposed to citrate-capped ultrasmall gold nanoparticles.[68]

The thickness of the water thin film formed within SLBs is a critical factor in the overall solidity of the sensors built on different supports. The computational model of Au(100)-SLB indicated a small number of Na^+ and Cl^- ions present within the water thin film whereas, Au(111)-SLB indicated no ions present within the thin water film with 0.7 nm thickness. This observation is consistent with the NaCl concentration specified in the VMD solvation procedure for smaller volumes. In SiO_2-SLB a double layer of ions was observed where SiO_2 surface is covered with Na^+ ions to neutralize the ionized SiO_2 surface which is consistent with the experimental observations. Supports with different surfaces and functionalization resulted distinctive interfacial water thicknesses. This observation hints at the presence of dissimilar interactions between the lipids and supports of SLBs (Figure S6). Distinct non-bonded interactions such as van der Waals (vdW) and coulomb interaction energies were obtained for the three different SLBs as a function of distance between the bilayer and the support (*D*). Here, the interaction energies do not follow the Lennard-Jones potential as the energies were recorded at the stabilized lipid-support distances only. The calculated vdW energies are largely negative suggesting a large attractive force. The DLVO interaction energies were obtained by setting the distance between the two surfaces for the SLBs at 1.5 nm. In contrast, calculated interaction energies were acquired considering shorter distances between the lipid and supports. The non-bonded interactions of Au(100) and Au(111)-SLBs consist only of vdW energies whereas, SiO_2-SLB consists of both vdW and coulomb interactions. Coulomb interactions obtained for the SiO_2-SLB is largely attractive and we believe it is caused by not including the effects coming from the Na^+ ions on the SiO_2 surfaces.

Substrate Effects on Protein Bilayer Interactions. To further investigate the potential for negatively charged SiO_2 preventing the adsorption of nanoscale analytes to SLBs, we observe the adsorption of cytochrome *c* to SLBs formed with the solvent-assisted method on SiO_2 *vs* Au surfaces. Figure 4 shows the frequency and dissipation change for 30 min of cytochrome *c* flow, followed by 30 min of static incubation, and rinse.

We find that cytochrome *c* does not interact with DOPC SLBs on SiO_2 surfaces, consistent with previous reports.[24] In contrast, we find that cytochrome *c* adsorbs to both bare SiO_2 and bare Au substrates. The frequency and dissipation change for cytochrome *c* adsorption to both bare substrates is the same (table S3; $p < 0.05$). Additionally, we find that cytochrome *c* adsorbs to DOPC SLBs formed on a Au surface. The magnitude of frequency change was increased for adsorption to SLBs formed on a Au surface as compared to bare SiO_2 or Au surfaces. The cytochrome *c* adsorption to bare SiO_2 and Au increased the dissipation by a small amount, consistent with adsorption of a thin layer of biological material.[24] Adsorption of cytochrome *c* to SLBs on Au surfaces has a significantly larger increase in dissipation. Increased dissipation associated with cytochrome *c*-SLB interaction is consistent with previous observation of cytochrome *c*-SLB interaction.[24]

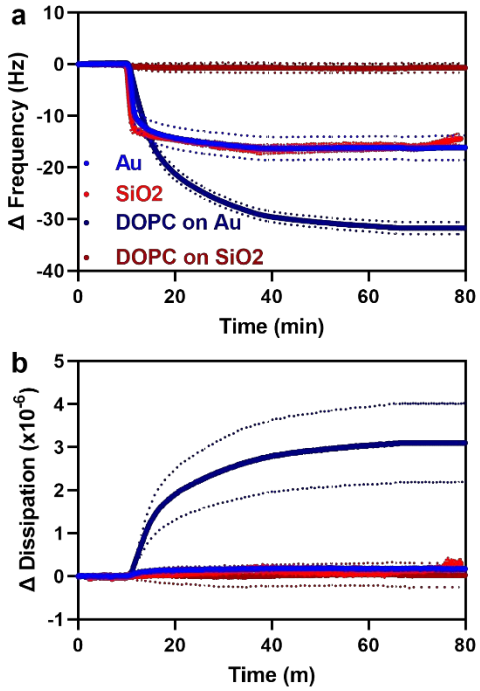

Figure 4. Change in (a) frequency and (b) dissipation *vs* time for interactions of cytochrome *c* with bare Au, bare SiO_2, DOPC bilayer formed on Au, and DOPC bilayer formed on SiO_2. All SLBs are formed with the solvent-assisted method. Dotted lines represent one standard deviation of four replicate measurements.

To further characterize the interaction of cytochrome *c* with DOPC SLBs on Au substrates, we perform a more detailed analysis of their binding kinetics. We first examine the dissipation change as a function of frequency change. Such plots are useful, for example, when attempting to differentiate between mechanisms of protein-bilayer interactions.[69] Figure 5a shows the dissipation change as a function of frequency change for cytochrome *c* interaction with bare SiO_2 and Au as well as DOPC SLBs on SiO_2 and Au substrates. For adsorption to either bare SiO_2 or Au substrates, frequency decreases along the *x* axis with little change in dissipation. This is indicative of a thin rigidly adsorbed film on the surface.[59] For adsorption to a DOPC bilayer on Au surface, the trace moves into the negative frequency-positive dissipation quadrant. This is indicative of protein adsorption to the bilayer adding both mass and altering bilayer viscoelastic properties. Cytochrome *c* has been shown to intercalate into a bilayer and alter lipid packing density and rigidity.[70]

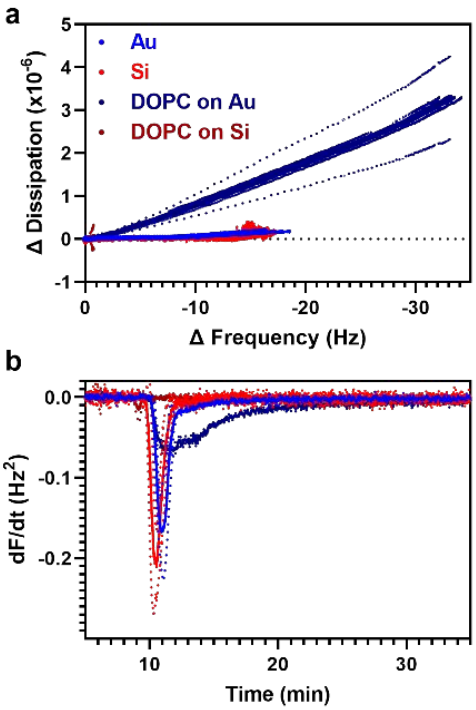

Figure 5. a) Change in frequency *vs* change in dissipation for cytochrome *c* interaction. Frequency change is graphed with a negative *x* axis. b) The first derivative of frequency change *vs* time. All SLBs are formed with the solvent-assisted method. Dotted lines represent one standard deviation of four replicate measurements.

To further distinguish the mechanism of cytochrome *c* interaction, we graph the first derivative of frequency change with respect to time (*dF/dt*) as a function of time. This highlights two important features of cytochrome *c* adsorption kinetics: 1) the maximum adsorption rate and 2) the length of the adsorption time. Both of these features can be used to determine whether the rate limiting step for adsorption is collision rate of protein with surface or a secondary process. Figure 5b shows the first derivative of frequency change with respect to time (*dF/dt*) *vs* time. The maximum adsorption rate for cytochrome *c* interaction with bare SiO_2 and Au do not differ ($p < 0.05$). The maximum adsorption rate for cytochrome *c* interaction with a DOPC bilayer on Au substrate is lower than the rate of adsorption to either bare substrate. This is indicative that the rate limiting step to cytochrome *c* adsorption to a DOPC SLB on Au substrate is not the collision rate of protein with the bilayer, as the adsorption rate would be equal to or greater than that of bare

substrates. The length of adsorption time for cytochrome *c* interaction with bare SiO_2 and Au substrates does not differ ($p < 0.05$). The length of the adsorption time for cytochrome *c* interaction with a DOPC bilayer on Au substrate is longer than the length of adsorption to either bare substrate. Taken together, we understand the adsorption process of cytochrome *c* to a DOPC bilayer on Au substrate to have a rate limiting step that is not the collision rate of protein with the bilayer.

Cytochrome *c* adsorption and stability on phospholipid bilayers depends on cytochrome *c* orientation and functional group interaction with phospholipids.[24–26] Our results are consistent with the rate limiting step of cytochrome *c* adsorption kinetics not being protein-bilayer collision, but instead being cytochrome *c* contact orientation. Previously, the zwitterionic DOPC headgroup was thought to be responsible for the lack of interaction between cytochrome c and DOPC SLBs;[24] however, our results show that cytochrome *c* can adsorb, and remain adsorbed, to a bilayer composed of only phosphatidylcholine headgroups. We speculate that the contact orientation of cytochrome *c* is impacted by the substrate under the bilayer. For a DOPC bilayer formed on a SiO_2 substrate, the contact orientation is heavily skewed towards an unfavorable adsorption orientation. For a DOPC bilayer formed on a Au substrate, the distribution of contact orientations is not skewed away from favorable adsorption interactions. This may explain why cytochrome *c* adsorbs to bilayers containing anionic lipid and not zwitterionic lipid on SiO_2 substrates. This does not explain the lack of binding in previously performed computational simulations.[24]

Simulations of Substrate Effects on Protein Bilayer Interactions. To contextualize QCM-D observations, we performed simulations of cytochrome c interacting with SLBs built on SiO_2 and Au substrates. The distribution in the positions of cytochrome *c* near the DOPC lipid bilayer in SLBs is reported using calculated protein densities (Figure 6) averaged across the corresponding ensemble of 80 ns molecular dynamics simulations. We found that the protein tends to be closer to the SiO_2-SLB than that of Au(100)-SLB (Figure 6d). Specifically, the peak of the distribution of positions of the protein is ~ 37 Å and ~49 Å to the lipid surfaces of SiO_2-SLB and Au(100)-SLB (Figure 6b, d), respectively. The protein densities near Au(111)-SLB lipid surface are different to those for Au(100)-SLB. Cytochrome *c* near Au(111)-SLB indicates closer interactions with

lipid bilayer than that of Au(100)-SLB, and provide a hint of a substrate effect coming from different surface terminations of gold. Interestingly, the protein densities near Au(100)-SLB have a similar protein density pattern with a ~2.5 Å shift compared to the control simulations; Au(100) support (Figure 6b). This suggests that cytochrome *c* interactions with Au(100)-SLB are predominantly governed by the support—viz Au(100)—with a slight repulsion by the SLB towards the cytochrome *c*. The probabilities of finding a protein near SLBs are different to those of DOPC lipid bilayer without any support. Considering the DOPC lipid bilayer without any support as the main control to compare with the SLBs, the synergetic effect from the lipid bilayer and support in Au(100)-SLB repel the cytochrome c away from the lipid surfaces while the synergetic effect of lipid bilayer and Au(111) or SiO_2 attracts protein towards the lipid surfaces of Au(111)-SLB and SiO_2-SLB.

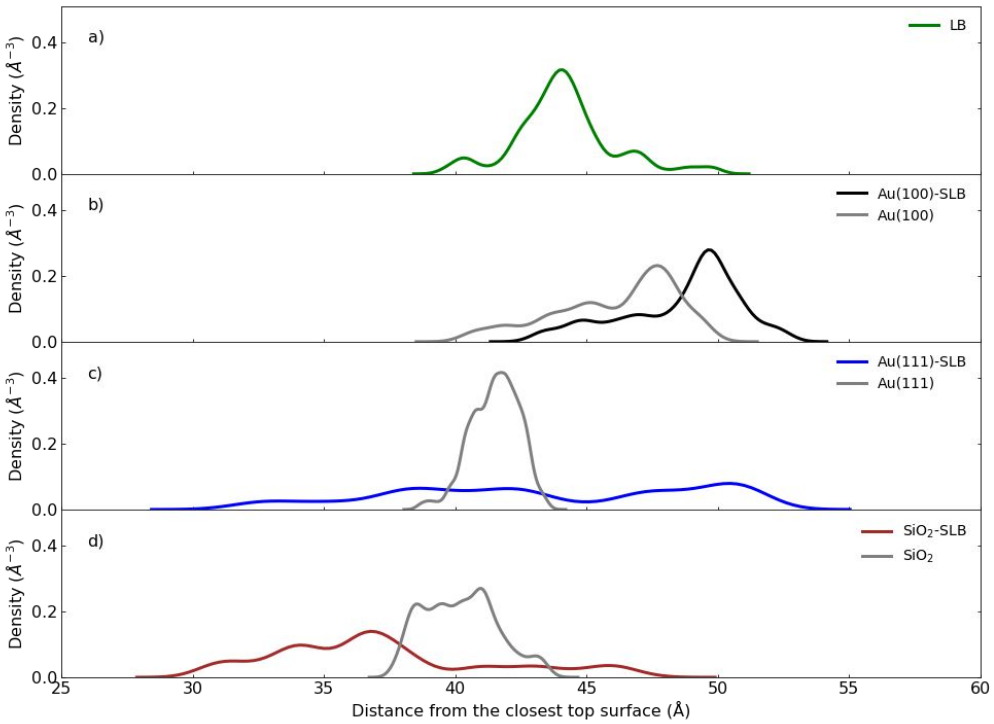

Figure 6. Averaged cytochrome *c* protein densities as a function of distance to the top-most surface observed during the equilibrating stage of the sampled nonequilibrium relaxations of the selected systems: a) DOPC lipid bilayer (LB) b) Au(100)-SLB c) Au(111)-SLB and d) SiO_2-SLB. The averaged cytochrome *c* protein densities as a function of the distance to the top-most surface (viz the closest top surface of the lipid bilayer for the SLB systems and the closest top surface of the Au or SiO_2 slabs); a) Au(100) b) Au(111 c) and d) SiO_2 controls are shown in grey color as a direct comparison with the protein densities in SLBs.

The protein densities in SLBs were compared to the protein densities in control experiments (Figure 6 b, c, d) where we simulated the cytochrome *c* on bare supports; Au(100), Au(111) and SiO_2. On the bare supports, the protein interacts closely with both the Au and SiO_2 bare surfaces as indicated by shorter distances (~35-50 Å) to the protein from the respective surfaces in comparison with the case with protein and DOPC lipid bilayer (Figure 6a). This observation partly supports the experimental observations of protein absorption to the bare Au and SiO_2 surfaces. However, cytochrome *c* interacts more closely with Au(111)-SLB and SiO_2-SLB surfaces than their respective bare surfaces.

Cytochrome *c* can interact with lipid bilayers through different binding sites. The A, C L and N[47] binding sites have been identified as the possible binding sites of cytochrome *c* with lipid bilayers. The A, C, L and N binding sites are composed of the [Lys], [Asn], [Lys, His], and [Phe, Gly, Thr, Trp, Lys] residues, respectively. The L site is composed of positive amino acids, C is composed of polar uncharged residues and N is a mix of hydrophobic, polar uncharged, and positive charged residues. The calculated averaged densities of the A, L, C, N sites of cytochrome *c* protein as a function of distance to the SLB lipid surfaces are available in Figure S7. In the Au(100)-SLB site, N and C face toward the DOPC bilayer top surface, and the N, L, and C sites face toward the surface in Au(111)-SLB and SiO_2-SLB

Simulations on different SLBs and control experiments confirmed a substrate effect on cytochrome *c* dynamics near the closest top surfaces of SLBs which is evidenced by the variation of the observed protein interacting distances from the closest top surfaces across the SLBs and pure lipid bilayers. Specifically, the thin films in Au(111)-SLB required fewer water molecules to equilibrate the SLB. Due to the smaller water volume trapped in-between the Au(111) surface and DOPC, we did not observe any Na^+ or Cl^- ions present therein. However, a small number of ions were found to be present in the water volume trapped in between the Au(100) surface and DOPC as the system equilibrated. It is possible that the origin of this relative stability is the structuring induced by the gold surface, but the simulations did not provide enough statistics to confirm this conjecture.

Substrate effects on the protein were evaluated by monitoring the hydrogen bonded and non-bonded interactions between the cytochrome *c* protein and the DOPC lipid bilayer at each time frame along the simulations using the VMD's NAMD energy plugin. Figure 7 displays the averaged non-bonded interactions; Coulomb (Elec E) and van der Waals (vdW) interactions obtained from the simulation trajectories for Au(100), Au(111) and SiO_2 SLBs in comparison with the control; and the DOPC lipid bilayer without any support. The interaction energies were plotted as a function of distance from the respective closest top surfaces to compare with the interactions obtained by DLVO theory. The positive Elec E values (Figure 7a) for all cases indicate a repulsion between the cytochrome *c* and the DOPC lipid bilayer. However, SiO_2-SLB reports smaller positive values for Elec E than the case with only DOPC lipid bilayer. The Au(111)-SLB indicates larger repulsion (larger positive Elec E) with the DOPC lipid bilayer compared to the case with the DOPC lipid bilayer. The vdW (Figure 7b) interaction energies vary within the same energy range as calculated in DLVO theory. Clearly, the cytochrome *c* demonstrates stronger vdW interactions with SiO_2-SLB or Au(111)-SLB than Au(100) -SLB or DOPC lipid bilayer without any support.

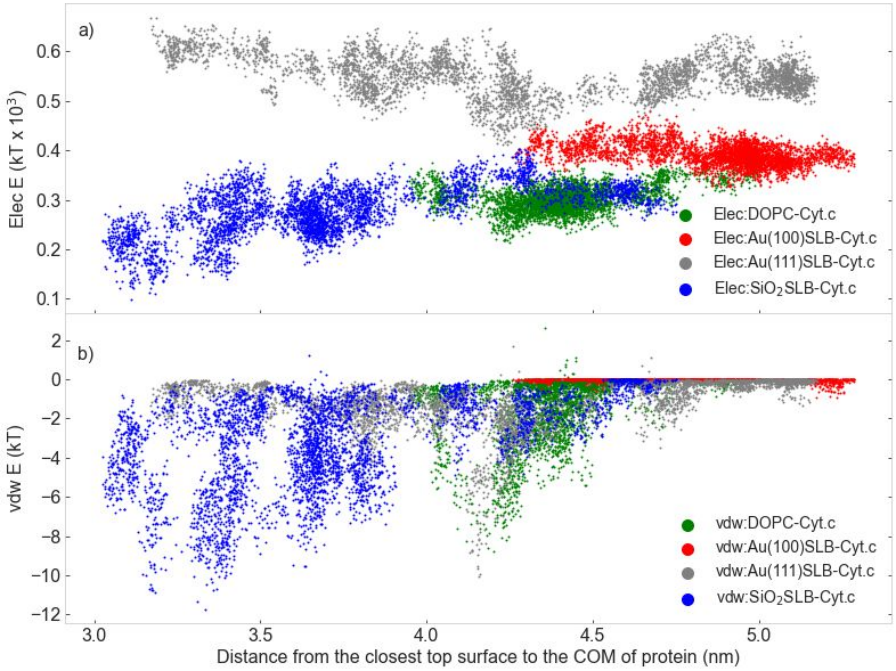

Figure 7. The non-bonded interactions between cytochrome *c* and DOPC lipid bilayer for the systems; DOPC lipid bilayer (green), Au(100)-SLB (red), Au(111)-SLB (grey), and SiO_2-SLB (blue) a) Electrostatic interactions (Elec) b) van der Waals (vdW) interactions.

Non-bonded interactions between cytochrome *c* and bare supports (Figure 8) were calculated to determine the forces that are responsible for the observed dynamics of cytochrome *c* near the different bare surfaces. Cytochrome *c* attracts to the Au(100) surface only through vdW interactions at zero Elec E. Similarly, cytochrome *c* attracts to the Au(111) bare surface through vdW interactions only when the attraction is larger than that of Au(100). On the other hand, cytochrome *c* does interact with bare SiO_2 through smaller vdW interactions. The Elec E of cytochrome *c* interacting with SiO_2 surface exhibits larger negative values. These values were calculated by considering the 13.3 % ionized SiO_2 surface without including the solvating effects coming from the Na^+ ions on the Si surface. Our simulations showed a double layer (layer of Na^+ ions) formed on the SiO_2 surface which is also observed in the experiments. The interactions between glass substrates and neutral bilayers can include the double layer interactions, hydration and hydrophobic interactions to reflect the correct interactions.[71] Thus, it appears that the larger negative attraction force we see for SiO_2 is due to not including the double layer interaction term in our calculation.

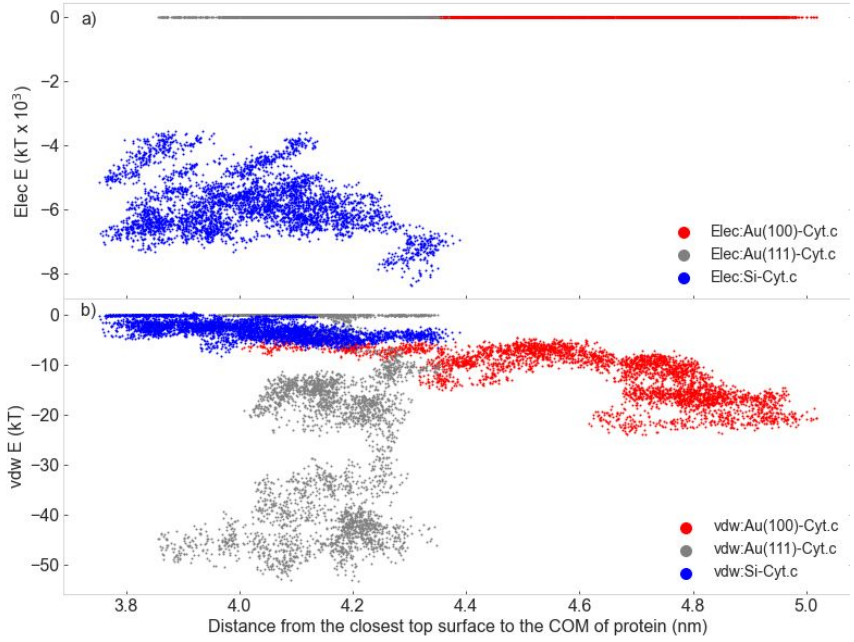

Figure 8. The non-bonded interactions between cytochrome *c* and supports for the control systems; Au(100), Au(111), and SiO_2 a) Electrostatic interactions (Elec) b) Van der Waals (vdW) interactions.

The relative percentage of hydrogen bonds occurring during the trajectory simulation time was also observed for the SLB and bare systems to identify if hydrogen bonded interactions play a role in the dynamics of cytochrome *c* near the surfaces, and are available in Figure S8 of the SM. Cytochrome *c* near SiO_2-SLB, Au(111)-SLB and SiO_2 exhibited hydrogen bonds during the simulation time. However, it was observed that hydrogen bonds contribute during a small percentage of the total simulation time. There were no hydrogen bonded interactions observed in the Au(100)-SLB systems, and the protein was only near the Au(100) and Au(111) bare surfaces during the simulations.

The structures of the cytochrome *c* protein near the SLB and bare systems were assessed to clarify any structural changes to the protein. They was monitored through the calculated radius of gyration (*R*g) of the cytochrome *c* during the simulations. The plotted *R*g as the density against the distance between protein and the closest top surface is available in Figure S9. The sampled population indicated the cytochrome *c* resides within a reasonable distance from the SLB and bare surfaces with a *R*g near the native value of 13.6 Å.[46]

CONCLUSIONS

We find that interactions between anionic MUA-AuNPs or cytochrome *c* and zwitterionic DOPC SLBs depend on the substrate beneath the supported lipid bilayer. We find that anionic MUA-AuNPs have increased adsorption to SLBs built on Au *vs.* SiO_2 surfaces. Using DLVO theory, we attribute the change in interaction for AuNPs to the increased Hamaker constant, and therefore increased van der Waals attractive interactions, for Au–Au interaction *vs.* SiO_2–Au interaction, as well as decreased Coulombic repulsion for neutral Au–anionic AuNP interaction *vs* anionic SiO_2–anionic AuNP interaction. Our application of DLVO theory suggests that we should see adsorption of AuNPs to a SLB on an SiO_2 substrate, which we do not see experimentally. We

hypothesize that this may be due to a number of forces that classical DLVO theory does not take into account, such as hydration or image charge.

We find that interactions between cytochrome *c* and DOPC SLBs are dependent on the substrate beneath the SLB. Cytochrome *c* has increased adsorption to DOPC SLBs built on Au *vs.* SiO_2 substrates, while cytochrome *c* does not have any difference in interaction with either bare substrate. Additionally, we find that the adsorption kinetics of cytochrome *c* to DOPC SLBs formed on Au surfaces are consistent with orientation limited stability of cytochrome *c* on membranes. We speculate that the presence of the SiO_2 layer beneath the bilayer preferentially biases the orientation of cytochrome *c* to an unfavorable adsorption angle.

The simulations of DOPC lipid bilayer on different substrates; (Au(100), Au(111), SiO_2) resulted in different thicknesses of water thin films in SLB models. Specifically, the DOPC lipid bilayer on Au(111) surface was stabilized with a lesser thickness (~0.7 nm) water thin film than the 1.5 nm water thickness speculated by experiments. The numerical measurements from computational simulations on SLBs indicated a substrate effect on cytochrome *c*-DOPC lipid bilayer interactions for Au vs. SiO_2 substrates compared to the case without any substrate underneath. Our calculations support the fact that the experiments were carried out on Au(111)-SLBs rather than the Au(100) surfaces as the cytochrome *c* does not show strong interactions with Au(100)-SLB or bare Au(100) substrate. We also observed strong interactions of cytochrome *c* with SiO_2-SLB which could be due to the same reason of seeing adsorption of AuNPs to a SLB on an SiO_2 substrate using DLVO theory. Cytochrome *c* exhibits relatively stronger interactions with bare Au(111) and SiO_2 surfaces compared to the DOPC lipid bilayer without any substrate which confirms the protein absorption on the bare Au and SiO_2 surfaces in QCM-D experiments. The protein densities were averaged by sampling different orientations of the protein at the beginning of simulations. Therefore, the broad range of protein densities observed for both Au(111) and SiO_2-SLBs could result from the preference of the cytochrome c orientations towards the SLBs. We found that cytochrome *c* interacts with SLBs through non-bonded interactions, vdW as the prime interaction component. The protein structure maintained its native state near the SLB surfaces.

Cationic NP–SLB interactions have received much attention due to the destructive nature of many cationic NP–bilayer interactions.[72,73] Anionic NP–bilayer interactions have been proven to be more subtle requiring sensitive model systems to understand mechanisms of interaction.[74] Recent studies have shown similarities in interaction mechanisms between cationic and anionic NPs and membranes, which highlight the ability of charged nanomaterial—anionic or cationic—to intercalate into biological membranes similarly to amino acids.[75–77] Due to the prevalence of metal oxide substrates, such as SiO_2, for NP–SLB interaction, some models have shown a lack of interaction, or significantly diminished interaction, between anionic nanoparticles and SLBs.[23,73] We speculate that in some of these cases the lack of interaction was due to substrate influence on NP behavior and not directly tied to unfavorable bilayer-NP interaction. We further hypothesize that the delineation of the potential interactions between anionic nanoparticles and SLBs on neutral substrates, such as Au, is useful for the characterization of negatively charged metal oxide substrates.

Moving forward, we welcome detailed characterization of the solvent assisted method of SLB formation and that for SLBs formed on varying substrates. The solvent-assisted method of SLB formation, in particular on Au substrates, has received relatively little attention as compared to the vesicle fusion method of SLB formation. The interfacial distance for SLBs formed on metal oxide substrates has been directly measured by small-angle neutron scattering.[78] Bilayer properties, such as compressibility and phase boundary height, for SLBs formed on metal oxide substrates have been measured by atomic force microscopy.[8] Additional measurement of SLB properties includes surface plasmon resonance, Fourier transform infrared spectroscopy, optical waveguide light mode sensing, etc. To fully understand interactions between nanoscale analytes and SLBs formed on varying substrates, and the degree to which these interactions accurately model biological systems, rigorous characterization of SLBs on any planned substrate is required.attention

AUTHOR CONTRIBUTIONS

Initial experimentation was conceived of by JAP and CARL. QCM-D experiments and analysis were completed by CARL. DLVO calculations were completed by CARL with assistance from TRG. Computational modeling was conceived by RH and RDS, and

completed by RDS with assistance from RAM and KT. MUA-AuNPs were synthesized by KNLH. The initial draft of the manuscript was written by CARL. The initial draft of the computational section was written by RDS. Editing of the manuscript was performed by CARL, RDS, CJM, RJH, JAP, and RH.

ACKNOWLEDGEMENTS

This work was supported by the National Science Foundation under grant no. CHE-2001611, the NSF Center for Sustainable Nanotechnology (CSN). The CSN is part of the Centers for Chemical Innovation Program. JAP acknowledges support from a Vilas Distinguished Achievement Professorship and the University of Wisconsin-Madison, Office of the Vice Chancellor for Research and Graduate Education with funding from the Wisconsin Alumni Research Foundation. C.A.R.L. acknowledges support from the University of Wisconsin – Madison College of Agriculture and Life Sciences. The computing resources necessary for this work were provided in part by the Advanced Cyberinfrastructure Coordination Ecosystem: Services & Support (ACCESS), which is supported by National Science Foundation (NSF) Grant Number ACI-1548562 through allocation CTS090079, and the Advanced Research Computing at Hopkins (ARCH) high-performance computing (HPC) facilities supported by NSF Grant Number OAC-1920103. RDS acknowledges Dr. Clyde A. Daly Jr. for offering initial analysis scripts for nanoparticles protein interactions and Dr. Jaime Combariza for technical support with the ARCH supercomputer.

REFERENCES

(1) Granéli, A.; Rydström, J.; Kasemo, B.; Höök, F. Formation of Supported Lipid Bilayer Membranes on SiO2 from Proteoliposomes Containing Transmembrane Proteins. *Langmuir* **2003**, *19* (3), 842–850. https://doi.org/10.1021/la026231w.

(2) Wang, K. F.; Nagarajan, R.; Mello, C. M.; Camesano, T. A. Characterization of Supported Lipid Bilayer Disruption By Chrysophsin-3 Using QCM-D. *J. Phys. Chem. B* **2011**, *115* (51), 15228–15235. https://doi.org/10.1021/jp209658y.

(3) Yousefi, N.; Tufenkji, N. Probing the Interaction between Nanoparticles and Lipid Membranes by Quartz Crystal Microbalance with Dissipation Monitoring . *Frontiers in Chemistry* . 2016, p 46.

(4) Castellana, E. T.; Cremer, P. S. Solid Supported Lipid Bilayers: From Biophysical Studies to Sensor Design. *Surf. Sci. Rep.* **2006**, *61* (10), 429–444. https://doi.org/10.1016/j.surfrep.2006.06.001.

(5) Zhang, M.; Soto-Rodríguez, J.; Chen, I.-C. C.; Akbulut, M. Adsorption and Removal Dynamics of Polymeric Micellar Nanocarriers Loaded with a Therapeutic Agent on Silica Surfaces. *Soft Matter* **2013**, *9* (42), 10155–10164. https://doi.org/10.1039/c3sm51692j.

(6) Reviakine, I.; Johannsmann, D.; Richter, R. P. Hearing What You Cannot See and Visualizing What You Hear: Interpreting Quartz Crystal Microbalance Data from Solvated Interfaces. *Anal. Chem.* **2011**, *83* (23), 8838–8848. https://doi.org/10.1021/ac201778h.

(7) Yin, H.; Mensch, A. C.; Lochbaum, C. A.; Foreman-ortiz, I. U.; Caudill, E. R.; Hamers, R. J.; Pedersen, J. A. Influence of Sensor Coating and Topography on Protein and Nanoparticle Interaction with Supported Lipid Bilayers. *Langmuir* **2021**, *37* (7), 2256–2267. https://doi.org/10.1021/acs.langmuir.0c02662.

(8) Melby, E. S.; Mensch, A. C.; Lohse, S. E.; Hu, D.; Orr, G.; Murphy, C. J.; Hamers, R. J.; Pedersen, J. A. Formation of Supported Lipid Bilayers Containing Phase-Segregated Domains and Their Interaction with Gold Nanoparticles. *Environ. Sci. Nano* **2016**, *3* (1), 45–55. https://doi.org/10.1039/c5en00098j.

(9) Verity, J. E.; Chhabra, N.; Sinnathamby, K.; Yip, C. M. Tracking Molecular Interactions in Membranes by Simultaneous ATR-FTIR-AFM. *Biophys. J.* **2009**, *97* (4), 1225–1231. https://doi.org/10.1016/j.bpj.2009.06.013.

(10) Sugihara, K.; Delai, M.; Szendro, I.; Guillaume-Gentil, O.; Vörös, J.; Zambelli, T. Simultaneous OWLS and EIS Monitoring of Supported Lipid Bilayers with the Pore Forming Peptide Melittin. *Sens. Actuators B Chem.* **2012**, *161* (1), 600–606. https://doi.org/10.1016/j.snb.2011.11.007.

(11) Liu, X.; Chen, K. L. Interactions of Graphene Oxide with Model Cell Membranes: Probing Nanoparticle Attachment and Lipid Bilayer Disruption. *Langmuir* **2015**, *31* (44), 12076–12086. https://doi.org/10.1021/acs.langmuir.5b02414.

(12) Kobayashi, T.; Kono, A.; Futagawa, M.; Sawada, K.; Tero, R. Formation and Fluidity Measurement of Supported Lipid Bilayer on Polyvinyl Chloride Membrane. *AIP Conf. Proc.* **2014**, *1585* (1), 145–152. https://doi.org/10.1063/1.4866633.

(13) Güldenhaupt, J.; Adigüzel, Y.; Kuhlmann, J.; Waldmann, H.; Kötting, C.; Gerwert, K. Secondary Structure of Lipidated Ras Bound to a Lipid Bilayer. *FEBS J.* **2008**, *275* (23), 5910–5918. https://doi.org/10.1111/j.1742-4658.2008.06720.x.

(14) Hernandez, M. R.; Towns, E. N.; Moore, J.; Lee, H.; German, J. B.; Lebrilla, C. B.; Parikh, A. N.; Land, D. P. Use of Attenuated Total Reflectance Fourier Transform Infrared Spectroscopy to Study Lactosylceramide and GD3 DMPC Bilayers. *Colloids Surf. B Biointerfaces* **2012**, *94*, 374–377. https://doi.org/10.1016/j.colsurfb.2012.01.034.

(15) Schwörer, F.; Trapp, M.; Ballauff, M.; Dahint, R.; Steitz, R. Surface-Active Lipid Linings under Shear Load—A Combined in-Situ Neutron Reflectivity and ATR-FTIR Study. *Langmuir* **2015**, *31* (42), 11539–11548. https://doi.org/10.1021/acs.langmuir.5b01678.

(16) Jackman, J. A.; Ferhan, A. R.; Cho, N.-J. J. Surface-Based Nanoplasmonic Sensors for Biointerfacial Science Applications. *Bull. Chem. Soc. Jpn.* **2019**, *92* (8), 1404–1412. https://doi.org/10.1246/bcsj.20190112.

(17) Cho, N.-J. J.; Frank, C. W.; Kasemo, B.; Höök, F. Quartz Crystal Microbalance with Dissipation Monitoring of Supported Lipid Bilayers on Various Substrates. *Nat. Protoc.* **2010**, *5* (6), 1096–1106. https://doi.org/10.1038/nprot.2010.65.

(18) Jackman, J. A.; Cho, N. Supported Lipid Bilayer Formation: Beyond Vesicle Fusion. *Langmuir* **2020**, *36* (6), 1387–1400. https://doi.org/10.1021/acs.langmuir.9b03706.

(19) Ferhan, A. R.; Yoon, B. K.; Park, S.; Sut, T. N.; Chin, H.; Park, J. H.; Jackman, J. A.; Cho, N.-J. J. Solvent-Assisted Preparation of Supported Lipid Bilayers. *Nat. Protoc.* **2019**, *14* (7), 2091–2118. https://doi.org/10.1038/s41596-019-0174-2.

(20) Su, H.; Liu, H.-Y. Y.; Pappa, A.-M. M.; Hidalgo, T. C.; Cavassin, P.; Inal, S.; Owens, R. M.; Daniel, S. Facile Generation of Biomimetic-Supported Lipid Bilayers on Conducting Polymer Surfaces for Membrane Biosensing. *ACS Appl. Mater. Interfaces* **2019**, *11* (47), 43799–43810. https://doi.org/10.1021/acsami.9b10303.

(21) Michalak, D. J.; Lösche, M.; Hoogerheide, D. P. Charge Effects Provide Ångström-Level Control of Lipid Bilayer Morphology on Titanium Dioxide Surfaces. *Langmuir* **2021**, *37* (13), 3970–3981. https://doi.org/10.1021/acs.langmuir.1c00214.

(22) Alkilany, A. M.; Lohse, S. E.; Murphy, C. J. The Gold Standard: Gold Nanoparticle Libraries To Understand the Nano–Bio Interface. *Acc. Chem. Res.* **2013**, *46* (3), 650–661. https://doi.org/10.1021/ar300015b.

(23) Chong, G.; Foreman-Ortiz, I. U.; Wu, M.; Bautista, A.; Murphy, C. J.; Pedersen, J. A.; Hernandez, R. Defects in Self-Assembled Monolayers on Nanoparticles Prompt Phospholipid Extraction and Bilayer-Curvature-Dependent Deformations. *J. Phys. Chem. C* **2019**, *123* (45), 27951–27958. https://doi.org/10.1021/acs.jpcc.9b08583.

(24) Melby, E. S.; Allen, C.; Foreman-Ortiz, I. U.; Caudill, E. R.; Kuech, T. R.; Vartanian, A. M.; Zhang, X.; Murphy, C. J.; Hernandez, R.; Pedersen, J. A. Peripheral Membrane Proteins Facilitate Nanoparticle Binding at Lipid Bilayer Interfaces. *Langmuir* **2018**, *34* (36), 10793–10805. https://doi.org/10.1021/acs.langmuir.8b02060.

(25) Zhou, J.; Zheng, J.; Jiang, S. Molecular Simulation Studies of the Orientation and Conformation of Cytochrome c Adsorbed on Self-Assembled Monolayers. *J. Phys. Chem. B* **2004**, *108* (45), 17418–17424. https://doi.org/10.1021/jp038048x.

(26) Rabe, M.; Verdes, D.; Seeger, S. Understanding Protein Adsorption Phenomena at Solid Surfaces. *Adv. Colloid Interface Sci.* **2011**, *162* (1), 87–106. https://doi.org/10.1016/j.cis.2010.12.007.

(27) Reed, J. C. Cytochrome c: Can't Live with It - Can't Live without It. *Cell* **1997**, *91* (5), 559–562. https://doi.org/10.1016/S0092-8674(00)80442-0.

(28) Choi, E. J.; Dimitriadis, E. K. Cytochrome c Adsorption to Supported, Anionic Lipid Bilayers Studied via Atomic Force Microscopy. *Biophys. J.* **2004**, *87* (5), 3234–3241. https://doi.org/10.1529/biophysj.104.047738.

(29) Schweitzer-Stenner, R. Relating the Multi-Functionality of Cytochrome c to Membrane Binding and Structural Conversion. *Biophys. Rev.* **2018**, *10* (4), 1151–1185. https://doi.org/10.1007/s12551-018-0409-4.

(30) Hernandez, R.; Popov, A. V. Molecular Dynamics out of Equilibrium: Mechanics and Measurables. *WIREs Comput. Mol. Sci.* **2014**, *4* (6), 541–561. https://doi.org/10.1002/wcms.1190.

(31) Cui, Q.; Hernandez, R.; Mason, S. E.; Frauenheim, T.; Pedersen, J. A.; Geiger, F. Sustainable Nanotechnology: Opportunities and Challenges for Theoretical/Computational Studies. *J. Phys. Chem. B* **2016**, *120* (30), 7297–7306. https://doi.org/10.1021/acs.jpcb.6b03976.

(32) Piella, J.; Bastús, N. G.; Puntes, V. Size-Controlled Synthesis of Sub-10-Nanometer Citrate-Stabilized Gold Nanoparticles and Related Optical Properties. *Chem. Mater.* **2016**, *28* (4), 1066–1075. https://doi.org/10.1021/acs.chemmater.5b04406.

(33) Haiss, W.; Thanh, N. T. K.; Aveyard, J.; Fernig, D. G. Determination of Size and Concentration of Gold Nanoparticles from UV-Vis Spectra. *Anal. Chem.* **2007**, *79* (11), 4215–4221. https://doi.org/10.1021/ac0702084.

(34) Bhattacharjee, S. DLS and Zeta Potential – What They Are and What They Are Not? *J. Controlled Release* **2016**, *235*, 337–351. https://doi.org/10.1016/j.jconrel.2016.06.017.

(35) Lowry, G. V; Hill, R. J.; Harper, S.; Rawle, A. F.; Hendren, C. O.; Klaessig, F.; Nobbmann, U. Environmental Science Nano Guidance to Improve the Scientific Value of Zeta- Potential Measurements in NanoEHS. **2016**, 953–965. https://doi.org/10.1039/c6en00136j.

(36) Penfold, J.; Staples, E.; Tucker, I. On the Consequences of Surface Treatment on the Adsorption of Nonionic Surfactants at the Hydrophilic Silica - Solution Interface. **2002**, No. 12, 2967–2970.

(37) Keller, C. A.; Kasemo, B. Surface Specific Kinetics of Lipid Vesicle Adsorption Measured with a Quartz Crystal Microbalance. *Biophys. J.* **1998**, *75* (3), 1397–1402. https://doi.org/10.1016/S0006-3495(98)74057-3.

(38) Krozera, A.; Rodahl, M. X-Ray Photoemission Spectroscopy Study of UV / Ozone Oxidation of Au under Ultrahigh Vacuum Conditions. *J. Vac. Sci. Technol.* **1996**, *1704* (September 1996).

(39) Tabaei, S. R.; Choi, J.-H. H.; Haw Zan, G.; Zhdanov, V. P.; Cho, N.-J. J. Solvent-Assisted Lipid Bilayer Formation on Silicon Dioxide and Gold. *Langmuir* **2014**, *30* (34), 10363–10373. https://doi.org/10.1021/la501534f.

(40) Hahn, M. W.; O'Melia, C. R. Deposition and Reentrainment of Brownian Particles in Porous Media under Unfavorable Chemical Conditions: Some Concepts and Applications. *Environ. Sci. Technol.* **2004**, *38* (1), 210–220. https://doi.org/10.1021/es030416n.

(41) Van Oss, C. J. *Interfacial Forces in Aqueous Media*, 2nd ed.; CRC Press, 2006.

(42) Hogg, R.; Healy, T. W.; Fuerstenau, D. W. Mutual Coagulation of Colloidal Dispersions. *Trans. Faraday Soc.* **1966**, *62* (615), 1638–1651. https://doi.org/10.1039/tf9666201638.

(43) Oleson, T. A.; Sahai, N. Interaction Energies between Oxide Surfaces and Multiple Phosphatidylcholine Bilayers from Extended-DLVO Theory. *J. Colloid Interface Sci.* **2010**, *352* (2), 316–326. https://doi.org/10.1016/j.jcis.2010.08.056.

(44) Hahn, M. W.; Abadzic, D.; O'Melia, C. R. Aquasols: On the Role of Secondary Minima. *Environ. Sci. Technol.* **2004**, *38* (22), 5915–5924. https://doi.org/10.1021/es049746d.

(45) Chen, Q.; Xu, S.; Liu, Q.; Masliyah, J.; Xu, Z. QCM-D Study of Nanoparticle Interactions. *Adv. Colloid Interface Sci.* **2016**, *233*, 94–114. https://doi.org/10.1016/j.cis.2015.10.004.

(46) Kataoka, M.; Hagihara, Y.; Mihara, K.; Goto, Y. Molten Globule of Cytochrome c Studied by Small Angle X-Ray Scattering. *J. Mol. Biol.* **1993**, *229* (3), 591–596. https://doi.org/10.1006/jmbi.1993.1064.

(47) Daly, C. A. Jr.; Allen, C.; Rozanov, N.; Chong, G.; Melby, E. S.; Kuech, T. R.; Lohse, S. E.; Murphy, C. J.; Pedersen, J. A.; Hernandez, R. Surface Coating Structure and Its Interaction with Cytochrome c in EG6-Coated Nanoparticles Varies with Surface Curvature. *Langmuir* **2020**, *36* (18), 5030–5039. https://doi.org/10.1021/acs.langmuir.0c00681.

(48) Wu, E. L.; Cheng, X.; Jo, S.; Rui, H.; Song, K. C.; Dávila-Contreras, E. M.; Qi, Y.; Lee, J.; Monje-Galvan, V.; Venable, R. M.; Klauda, J. B.; Im, W. CHARMM-GUI Membrane Builder toward Realistic Biological Membrane Simulations. *J. Comput. Chem.* **2014**, *35* (27), 1997–2004. https://doi.org/10.1002/jcc.23702.

(49) Choi, Y. K.; Kern, N. R.; Kim, S.; Kanhaiya, K.; Afshar, Y.; Jeon, S. H.; Jo, S.; Brooks, B. R.; Lee, J.; Tadmor, E. B.; Heinz, H.; Im, W. CHARMM-GUI Nanomaterial Modeler for Modeling and Simulation of Nanomaterial Systems. *J. Chem. Theory Comput.* **2022**, *18* (1), 479–493. https://doi.org/10.1021/acs.jctc.1c00996.

(50) Jo, S.; Kim, T.; Iyer, V. G.; Im, W. CHARMM-GUI: A Web-Based Graphical User Interface for CHARMM. *J. Comput. Chem.* **2008**, *29* (11), 1859–1865. https://doi.org/10.1002/jcc.20945.

(51) Humphrey, W.; Dalke, A.; Schulten, K. VMD: Visual Molecular Dynamics. *J. Mol. Graph.* **1996**, *14* (1), 33–38. https://doi.org/10.1016/0263-7855(96)00018-5.

(52) Martínez, L.; Andrade, R.; Birgin, E. G.; Martínez, J. M. PACKMOL: A Package for Building Initial Configurations for Molecular Dynamics Simulations. *J. Comput. Chem.* **2009**, *30* (13), 2157–2164. https://doi.org/10.1002/jcc.21224.

(53) Price, D. J.; Brooks, C. L., III. A Modified TIP3P Water Potential for Simulation with Ewald Summation. *J. Chem. Phys.* **2004**, *121* (20), 10096–10103. https://doi.org/10.1063/1.1808117.

(54) Phillips, J. C.; Braun, R.; Wang, W.; Gumbart, J.; Tajkhorshid, E.; Villa, E.; Chipot, C.; Skeel, R. D.; Kalé, L.; Schulten, K. Scalable Molecular Dynamics with NAMD. *J. Comput. Chem.* **2005**, *26* (16), 1781–1802. https://doi.org/10.1002/jcc.20289.

(55) Brooks, B. R.; Brooks III, C. L.; Mackerell Jr., A. D.; Nilsson, L.; Petrella, R. J.; Roux, B.; Won, Y.; Archontis, G.; Bartels, C.; Boresch, S.; Caflisch, A.; Caves, L.; Cui, Q.; Dinner, A. R.; Feig, M.; Fischer, S.; Gao, J.; Hodoscek, M.; Im, W.; Kuczera, K.; Lazaridis, T.; Ma, J.; Ovchinnikov, V.; Paci, E.; Pastor, R. W.; Post, C. B.; Pu, J. Z.; Schaefer, M.; Tidor, B.; Venable, R. M.; Woodcock, H. L.; Wu, X.; Yang, W.; York, D. M.; Karplus, M. CHARMM: The Biomolecular Simulation Program. *J. Comput. Chem.* **2009**, *30* (10), 1545–1614. https://doi.org/10.1002/jcc.21287.

(56) Heinz, H.; Lin, T.-J.; Kishore Mishra, R.; Emami, F. S. Thermodynamically Consistent Force Fields for the Assembly of Inorganic, Organic, and Biological Nanostructures: The INTERFACE Force Field. *Langmuir* **2013**, *29* (6), 1754–1765. https://doi.org/10.1021/la3038846.

(57) S. van der Walt; S. C. Colbert; G. Varoquaux. The NumPy Array: A Structure for Efficient Numerical Computation. *Comput. Sci. Eng.* **2011**, *13* (2), 22–30. https://doi.org/10.1109/MCSE.2011.37.

(58) Kluyver, T.; Ragan-Kelley, B.; Prez, F.; Granger, B.; Bussonnier, M.; Frederic, J.; Kelley, K.; Hamrick, J.; Grout, J.; Corlay, S.; Ivanov, P.; Avila, D.; Abdalla, S.; Willing, C.; Jupyter development team. Jupyter Notebooks ? A Publishing Format for Reproducible Computational Workflows; Loizides, F., Scmidt, B., Eds.; IOS Press, 2016; pp 87–90.

(59) Plunkett, M. A.; Claesson, P. M.; Ernstsson, M.; Rutland, M. W. Comparison of the Adsorption of Different Charge Density Polyelectrolytes: A Quartz Crystal Microbalance and X-Ray Photoelectron Spectroscopy Study. *Langmuir* **2003**, *19* (11), 4673–4681. https://doi.org/10.1021/la026569q.

(60) Lochbaum, C. A.; Chew, A. K.; Zhang, X.; Rotello, V.; Lehn, R. C. Van; Pedersen, J. A.; Van Lehn, R. C.; Pedersen, J. A. Lipophilicity of Cationic Ligands Promotes Irreversible Adsorption of Nanoparticles to Lipid Bilayers. *ACS Nano* **2021**, *15* (4), 6562–6572. https://doi.org/10.1021/acsnano.0c09732.

(61) Begtrup, G. E.; Gannett, W.; Yuzvinsky, T. D.; Crespi, V. H.; Zettl, A. Nanoscale Reversible Mass Transport for Archival Memory. *Nano Lett.* **2009**, *9* (5), 1835–1838. https://doi.org/10.1021/nl803800c.

(62) Wang, J.; Ocko, B. M.; Davenport, A. J.; Isaacs, H. S. Surface Charge-Induced Ordering of the Au(111) Surface. *Science* **1992**, *255* (5050), 1416–1418.

(63) Geada, I. L.; Ramezani-dakhel, H.; Jamil, T.; Sulpizi, M.; Heinz, H. Insight into Induced Charges at Metal Surfaces and Potential. *Nat. Commun.* No. 2018, 1–14. https://doi.org/10.1038/s41467-018-03137-8.

(64) Kane, V.; Mulvaney, P. Double-Layer Interactions between Self-Assembled Monolayers of ω-Mercaptoundecanoic Acid on Gold Surfaces. *Langmuir* **1998**, *14* (12), 3303–3311. https://doi.org/10.1021/la971296y.

(65) Eom, N.; Parsons, D. F.; Craig, V. S. J. Roughness in Surface Force Measurements: Extension of DLVO Theory To Describe the Forces between Hafnia Surfaces. *J. Phys. Chem. B* **2017**, *121* (26), 6442–6453. https://doi.org/10.1021/acs.jpcb.7b03131.

(66) Gabovich, A. M.; Gun'ko, V. M.; Klymenko, V. E.; Voitenko, A. I. Role of Dipole Image Forces in Molecular Adsorption. *Eur. Phys. J. B* **2012**, *85* (8), 284. https://doi.org/10.1140/epjb/e2012-30475-5.

(67) Son, C. Y.; Wang, Z.-G. Image-Charge Effects on Ion Adsorption near Aqueous Interfaces. *Proc. Natl. Acad. Sci.* **2021**, *118* (19), e2020615118. https://doi.org/10.1073/pnas.2020615118.

(68) Kariuki, R.; Penman, R.; Bryant, S. J.; Orrell-Trigg, R.; Meftahi, N.; Crawford, R. J.; McConville, C. F.; Bryant, G.; Voïtchovsky, K.; Conn, C. E.; Christofferson, A. J.; Elbourne, A. Behavior of Citrate-Capped Ultrasmall Gold Nanoparticles on a Supported Lipid Bilayer Interface at Atomic Resolution. *ACS Nano* **2022**, *16* (10), 17179–17196. https://doi.org/10.1021/acsnano.2c07751.

(69) Dixon, M. C. Quartz Crystal Microbalance with Dissipation Monitoring: Enabling Real-Time Characterization of Biological Materials and Their Interactions. *J. Biomol. Tech. JBT* **2008**, *19* (3), 151–158.

(70) Trusova, V. M.; Gorbenko, G. P.; Molotkovsky, J. G.; Kinnunen, P. K. J. Cytochrome C-Lipid Interactions: New Insights from Resonance Energy Transfer. *Biophys. J.* **2010**, *99* (6), 1754–1763. https://doi.org/10.1016/j.bpj.2010.06.017.

(71) Anderson, T. H.; Min, Y.; Weirich, K. L.; Zeng, H.; Fygenson, D.; Israelachvili, J. N. Formation of Supported Bilayers on Silica Substrates. *Langmuir* **2009**, *25* (12), 6997–7005. https://doi.org/10.1021/la900181c.

(72) Basak, U. K.; Roobala, C.; Basu, J. K. Size-Dependent Interaction of Hydrophilic / Hydrophobic Ligand Functionalized Cationic and Anionic Nanoparticles with Lipid Bilayers. **2020**.

(73) Tatur, S.; MacCarini, M.; Barker, R.; Nelson, A.; Fragneto, G. Effect of Functionalized Gold Nanoparticles on Floating Lipid Bilayers. *Langmuir* **2013**, *29* (22), 6606–6614. https://doi.org/10.1021/la401074y.

(74) Foreman-ortiz, I. U.; Liang, D.; Laudadio, E. D.; Calderin, J. D.; Wu, M.; Keshri, P.; Zhang, X.; Schwartz, M. P.; Hamers, R. J.; Rotello, V. M.; Murphy, C. J.; Cui, Q.; Pedersen, J. A. Anionic Nanoparticle-Induced Perturbation to Phospholipid Membranes Affects Ion Channel Function. *Proc. Natl. Acad. Sci.* **2020**, *117* (45), 27854 LP – 27861. https://doi.org/10.1073/pnas.2004736117.

(75) Canepa, E.; Salassi, S.; Simonelli, F.; Ferrando, R.; Rolandi, R.; Lambruschini, C.; Canepa, F.; Dante, S.; Relini, A.; Rossi, G. Non-Disruptive Uptake of Anionic and Cationic Gold Nanoparticles in Neutral Zwitterionic Membranes. *Sci. Rep.* **2021**, *11* (1), 1256. https://doi.org/10.1038/s41598-020-80953-3.

(76) Van Lehn, R. C.; Alexander-Katz, A. Grafting Charged Species to Membrane-Embedded Scaffolds Dramatically Increases the Rate of Bilayer Flipping. *ACS Cent. Sci.* **2017**, *3* (3), 186–195. https://doi.org/10.1021/acscentsci.6b00365.

(77) Wang, Y.; Hu, D.; Wei, D. Transmembrane Permeation Mechanism of Charged Methyl Guanidine. *J. Chem. Theory Comput.* **2014**, *10* (4), 1717–1726. https://doi.org/10.1021/ct400738r.

(78) Balgavý, P.; Dubničková, M.; Kučerka, N.; Kiselev, M. A.; Yaradaikin, S. P.; Uhŕíková, D.; Uhríková, D. Bilayer Thickness and Lipid Interface Area in Unilamellar Extruded 1,2-Diacylphosphatidylcholine Liposomes: A Small-Angle Neutron Scattering Study. *Biochim. Biophys. Acta BBA - Biomembr.* **2001**, *1512* (1), 40–52. https://doi.org/10.1016/S0005-2736(01)00298-X.